Permian magnetostratigraphy and end of the Kiaman Reverse Polarity Superchron from the southeast Karoo basin, South Africa.

De Kock, M.O.*, **Abubakre, A.O.**

DSI-NRF Centre of Excellence for Integrated Mineral and Energy Resource Analysis, Department of Geology, University of Johannesburg, PO Box 524, Auckland Park 2006, South Africa

Key points

- The end of the Kiaman Reverse Polarity Superchron is identified in the southeast Karoo basin allowing regional correlation
- The effect of Karoo large igneous province dolerite intrusions is limited, and primary Permian remanence define magnetostratigraphy
- The diachronous boundary between the Ecca and Beaufort groups is calibrated

Abstract

Paleomagnetic results and a ~2353 m-thick magnetostratigraphic section for undeformed late to early Permian rocks in the south-eastern part of the Karoo basin of South Africa are reported. Pseudo-single domain or single domain titanomagnetite as well as pyrrhotite were identified as possible remanence carriers of a dual polarity magnetization interpreted as the record of the Permian geomagnetic field during the Kiaman Reverse Polarity Superchron and subsequent Illawara mixed polarity zone. The timing of remanence acquisition is further constrained by the effect of Jurassic-aged dolerite intrusions, which either partially or wholly overprint the Permian remanence in their immediate vicinity. A paleopole at 53.2°S; 46.9°E and dp/dm = 5.9°/6.3° is calculated from the bedding-corrected primary remanence corrected for the effects of inclination shallowing using a correction factor of f = 0.6. This is comparable to known Permian paleopoles from the southwestern Karoo basin and overlaps with the 290-230 Ma segment of the Gondwana apparent polar wander path. The end of the Kiaman Reverse Polarity Superchron can be correlated between the extremes of the southern Karoo basin and reveal a diachronous boundary between the Ecca and the Beaufort groups that is calibrated for the first time.

Plain Language Summary

Magnetostratigraphy is used as a dating tool for calibrating the correlation of middle to late Permian sedimentary rock units. During the Permian, the Kiaman Reverse Polarity Superchron is a prominent ca. 318 Ma to 265 Ma magnetostratigraphic interval of reverse polarity described from east Australia and is followed by the Illawara interval of mixed polarity. The end of the Kiaman Reverse Polarity Superchron is a useful chronostratigraphic marker horizon. We identify the end of the Kiaman Reverse Polarity Superchron within drill core from the southeast Karoo basin and correlate this to its record within the southwest of that basin at localities that are 900 km apart. Another prominent marker horizon in the Karoo basin (i.e., the boundary between the Ecca and the Beaufort groups) is characterized by a change in depositional environment. That is a change from a marine environment to deposition in a terrestrial environment. Although this important lithostratigraphic boundary is known to be diachronous across the Karoo basin, we here illustrate and calibrate the degree of time transgression of this boundary in the southern part of the basin.

Index terms

1520 Magnetostratigraphy; 1535 Reversals: process,
timescale, magnetostratigraphy; 1540 Rock and mineral magnetism

Keywords

Magnetostratigraphy; Permian; Kiaman Reversed Polarity Superchron; Karoo large igneous province; Karoo basin; Gondwana

1. Introduction

Within the southern part of the main Karoo basin, the late Carboniferous to mid-Jurassic Karoo Supergroup of South Africa (Figure 1) represents a 12 km-thick, laterally continuous, clastic sedimentary succession that was deposited in a retro-arc foreland setting in response to subduction and accretionary tectonics along the southwestern margin of Gondwana (Johnson et al., 1996; Johnson et al., 2006). During the Permian an interplay between regional tectonics, an icehouse to greenhouse climatic transition, and a marine incursion resulted in deepening of the southern main Karoo basin and deposition of the Ecca Group (Catuneanu et al., 2002; Cole, 1992).

The Ecca Group is well documented in the southwest section of the basin in terms of lithostratigraphy (Cole, 1992; Wickens, 1994), geochronology (Bangert et al., 1999; Belica et al., 2017a; Fildani et al., 2007; Fildani et al., 2009; Griffis et al., 2019; McKay et al., 2016; McKay et al., 2015; Turner, 1999) and magnetostratigraphy (Abubakre and De Kock, 2021; Belica et al., 2017a; Lanci et al., 2013; Tohver et al., 2015). It, however, remains underexplored in the southeast where outcrops are fewer, the lithofacies very different (Johnson, 2009), and the stratigraphy interrupted by dolerite sills of the ca. 183 Ma Karoo large igneous province (KLIP). Magnetostratigraphy can be used as a dating tool for calibrating the lithostratigraphic correlation of the Ecca Group across basin between the dated southwest and the undated southeast sections. For this the Kiaman Reverse Polarity Superchron is a prominent Paleozoic magnetostratigraphic interval. It is an interval of reverse polarity described from eastern Australia that extend from ca. 318 Ma to 267-265 Ma, followed by the Illawara interval of mixed polarity (Belica et al., 2017b; Cortrell et al., 2008; Irving, 1963; Irving and Parry, 1963). The end of the Kiaman Reverse Polarity Superchron is particularly useful as a chronological marker (Hounslow et al., 2016; Kirschvink et al., 2015). It has been assigned an approximate age of 267 Ma (Steiner, 2006) but recently it was constrained by Belica et al. (2017b) to coincide with the Wordian-Capitanian boundary at ~265 Ma (Figure 2). In the southwest Karoo basin, Lanci et al. (2013) identified normal polarity intervals within the Waterford Formation of the Ecca Group and the Abrahamskraal Formation of the Beaufort Group, thus placing these rocks in the Illawara mixed polarity interval with an mid-Wordian age, based magnetostratigraphic age assignements of Steiner (2006). This was incorporated in the latest Permian magnetostratigraphy of

Hounslow and Balabanov (2018) (Figure 2), but the age assignments can now be revised to approximate the Wordian-Capitanian boundary based on the work of Belica et al. (2017b).

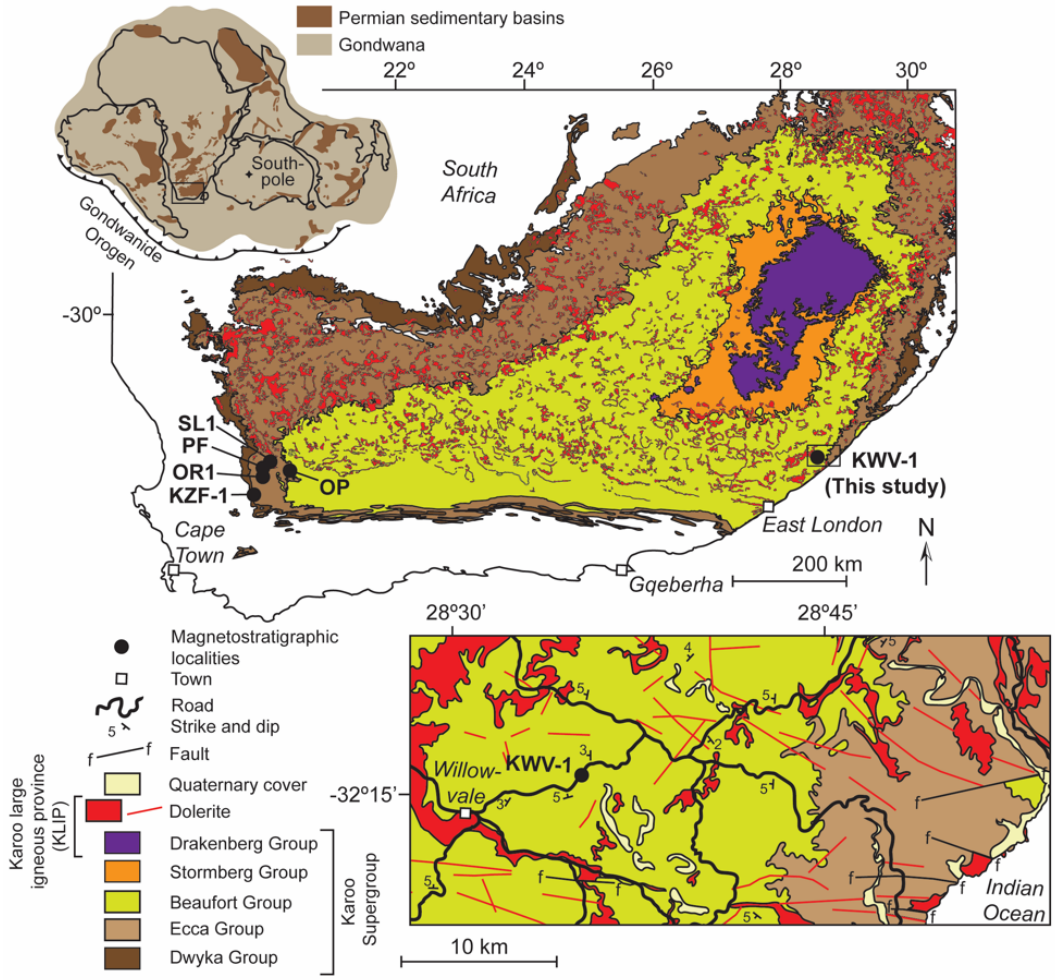

Figure 1. Simplified geology of the main Karoo basin of South Africa and locality of borehole KWV-1 (i.e., enlarged inset from the 1:250 000 3228 Kei Mouth map sheet) shown in relation to published magnetostratigraphic localities (modified from the 1:1 000 000 geological map of South Africa, Council for Geoscience, 1997). OP = Ouberg Pass, PF = Pienaarsfontein. Top left inset illustrates an Early Permian reconstruction of Gondwana with sedimentary basins (modified from Sirevaag et al., 2018).

Here, an integrated rock magnetic and paleomagnetic approach is used to study a 2353 m-long intersection (KWV-1) of the Ecca Group and dolerite intrusions from the southeastern main Karoo basin. The magnetic and thermal effect of the KLIP intrusions on surrounding sedimentary rocks are characterized and magnetostratigraphic

constraints are presented for the Ecca Group and lower Beaufort Group to assist lithostratigraphic correlation between extremes of the southern Karoo basin. The effects of KLIP intrusions on the Ecca Group are important to evaluate because carbonaceous mudstone units of the Ecca Group have been identified as a potential shale-gas resource (Decker, 2014; Decker and Marot, 2012; Kuuskraa et al., 2013). The scale of this resource, however, is unconstrained and depends amongst other factors on the lithostratigraphy of the Ecca Group throughout the basin and thermal effects associated with KLIP intrusions (Cole, 2014; De Kock et al., 2017; Mowzer and Adams, 2015).

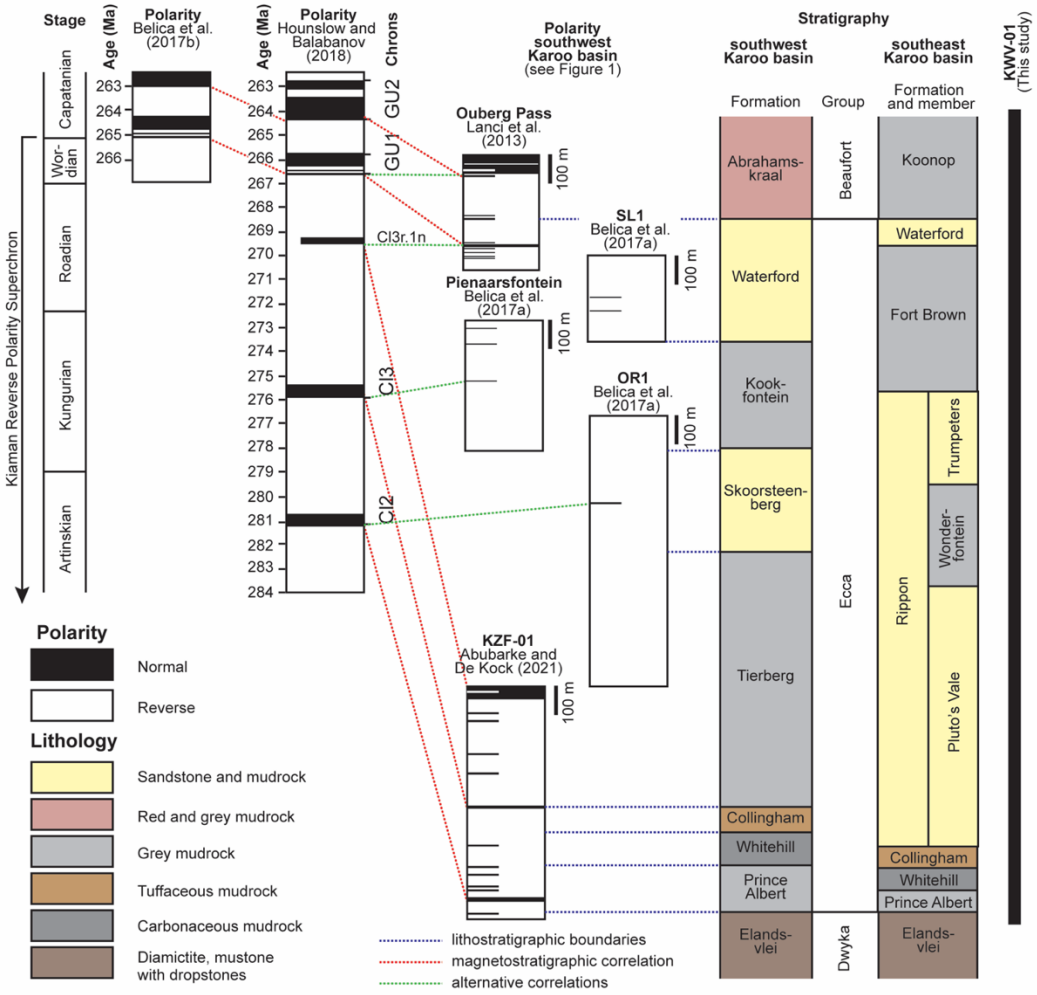

Figure 2. Mid and late Permian composite magnetostratigraphy of Hounslow and Balabanov (2018) and corrected chronology of the end of the Kiaman Reversed Polarity Superchron by Belica et al. (2017b) compared to magnetostratigraphic constraints from the southwestern Karoo basin (see Figure 1 for localities) and stratigraphy of the Ecca Group (after Johnson, 2009). The stratigraphic position of borehole KWV-01 is indicated for comparison.

2. Geological setting

The Karoo basin fill commences with the glaciogenic Dwyka Group followed by the marine Ecca Group and the fluvial-deltaic Beaufort Group (Johnson et al., 2006). The subsequent clastic sedimentary sequence of the Stormberg Group reflects increasingly arid conditions (Bordy et al., 2004; Johnson et al., 1996) and ends abruptly with the rapid KLIP sill emplacement (Hastie et al., 2014; Jourdan et al., 2005) and eruption of the Drakensberg Group basalts (Figure 1).

KWV-1 (S 32°14'43.10" E 28° 35'08.10") was drilled near Willowvale, within a borrow pit for road aggregate, in the Amathole district in the Eastern Cape Province of South Africa in the southeast extreme of the main Karoo basin and within a network of multiple dolerite sills (Figure 1). Bedding in the core is variable, but generally near horizontal with an average dip to the northwest based on electrical dip meter readings (dip direction = 302°, dip = 2°). KWV-1 provides a continuous 2352.39 m-thick succession from the uppermost layers of the Dwyka Group (i.e., the Elandsvlei Formation, below 2331.7 m depth), the entire Ecca Group (subdivided into Prince Albert [2302.4-2331.7 m], Whitehill [2269.2-2302.4 m], Collingham [2002.4-2269.2 m], Ripon [742.8-2002.4 m], Fort Brown [262-742.8 m] and Waterford [241.8-262 m] formations) and the lowermost part of the Beaufort Group (i.e., Koonap Formation [0-241.8 m], Figure 3). The lithostratigraphy of the Ecca Group here stands in contrast to the southwestern part of the basin where the Tierberg Formation is developed above the Collingham Formation (Figure 2). The Ripon Formation, which occurs east of 22° consists of fine-grained greywacke turbidite beds of varying thicknesses and is subdivided into the Pluto's Vale Member sandstone (1388-2002.4 m), the Wonderfontein Member shale (948.1-1388 m), and the Trumpeter's Member sandstone (742.8-948.1 m; Figure 3). Another marked difference compared to the southwestern part of the basin, is the presence of numerous dolerite intrusions that intersect the clastic sedimentary rock succession. A 18.82 m-thick fine-grained dolerite intrudes the top of the Whitehill Formation with a sharp contact in KWV-1. The top of this dolerite intrudes sharply into the base of the 712.14 m-thick arenaceous Pluto's Vale Member of the Rippon Formation. The Pluto's Vale Member is further intersected six times by dolerite intrusions with a total cumulative thickness of 234.86 m. The argillaceous Wonderfontein Member is intruded by a 46.07 m-thick dolerite intrusion between

1249.79 and 1203.72 m. The Trumpeter's Member envelopes a 9.6 m-thick dolerite intrusion between 965.12 and 955.48 m. In the upper parts of the core, the Fort Brown Formation is cut by eight thin dolerite intrusions with a total cumulative thickness of 71.75 m, and the Koonap Formation is intruded by two dolerite sills (i.e., 34.87 m and 1.87m thick) between 127.11 and 92.24 m-depth, and between 16.57 and 14.7 m-depth.

3. Method

As the KWV-1 core was retrieved, pieces of core was fitted for continuity before being marked with a reference line and indicating the upward direction with an arrow head by the managing geologists at the drill site (e.g., Figure 3D). Where successive pieces of core could not be fitted for continuity due to excessive breaking or core loss the core was marked with two short parallel lines perpendicular to the reference line, a new reference line was then selected and drawn along the next section of continuous retrieved core. The core is thus made up of several sections of continuous rock intersection, with pieces of core from a section being oriented relative to each other. Such sections ranged from less than a meter to over 100 meters. Orientation of the reference line on any section was determined relative to the bedding dip azimuths intersected in the core and dip meter readings down the hole. Generally the orientation line coincided with bedding dip azimuth. Electronic dip meter logging was not possible beyond 2000 m due to hole collapse after core retrieval. Orientation of the reference line from here to the end of hole was attempted by using the average bedding in the core (i.e., 302°/2°). Core logging and sampling was done at the Council for Geosciences National Core Library at Donkerhoek, South Africa. Plug samples for paleomagnetic analyses were taken at ~3m intervals, but this spacing was reduced near dolerite contacts. A piece of core earmarked for sampling was first split along the reference line, before a paleomagnetic sample was plugged perpendicular to the core axis and from the right-hand half of the split core using a benchtop drill press. Plugs were labelled with their depth and their azimuth was marked along their upper margins. Plug azimuths are equal to the orientation of the reference line minus 90°. Samples were oriented and prepared into specimens for step-wise demagnetization at the paleomagnetism laboratories at the University of Johannesburg (UJ) and California

Institute of Technology (Caltech). Demagnetization consisted of low-intensity progressive alternating field (AF) demagnetization in three to four 25 mT steps up to 75 mT or 100 mT. Thermal demagnetization was achieved through stepwise heating in 20-25°C steps from 100°C to 600°C. All measurements of remanence were made using 2G Enterprises 755 or DC-4K superconducting rock magnetometers.

Remanence components were identified and quantified via principal component analysis (Kirschvink, 1980) using PaleoMag 3.2 (Jones, 2002) with individual components calculated from three or more points for line fits and four or more points for plane fits. Component fits were used in subsequent analysis if fits mean angular deviation (MAD) values of ≤ 15° for line fits and ≤ 20° for plane fits. Component means were calculated using PaleoMag 3.2, which employs the methodology of McFadden and McElhinny (1988) for the combination of line and plane fits. Component means were used to calculate virtual geomagnetic poles (VGPs) as per Butler (1992). The VGPs were visualized using GPlates 2.2 (Williams et al., 2012). Remanence components interpreted as being primary were used to develop a magnetostratigraphic record by considering the stratigraphic variation of declination, inclination and the corresponding VGP latitude of specimens.

Fourteen representative samples were subjected to a suite of rock magnetic experiments as described by Kirschvink et al. (2008). This includes progressive isothermal remanent magnetization (IRM) acquisition up to 1000 mT followed by progressive AF demagnetization, progressive anhysteretic remanent magnetization (ARM) acquisition with a variable direct current biasing field of 0 to 1 mT, an ARM version of the Lowrie-Fuller test (e.g., Johnson 1975), and a comparison of natural remanent magnetization (NRM) and ARM stability with IRM stability after Fuller et al. (2002). IRM acquisition curves were unmixed using the MAX Unmix software (Maxbauer et al., 2016), which employs a skewed-normal distribution (Wuertz and Chalabi, 2015) to represent individual coercivity components.

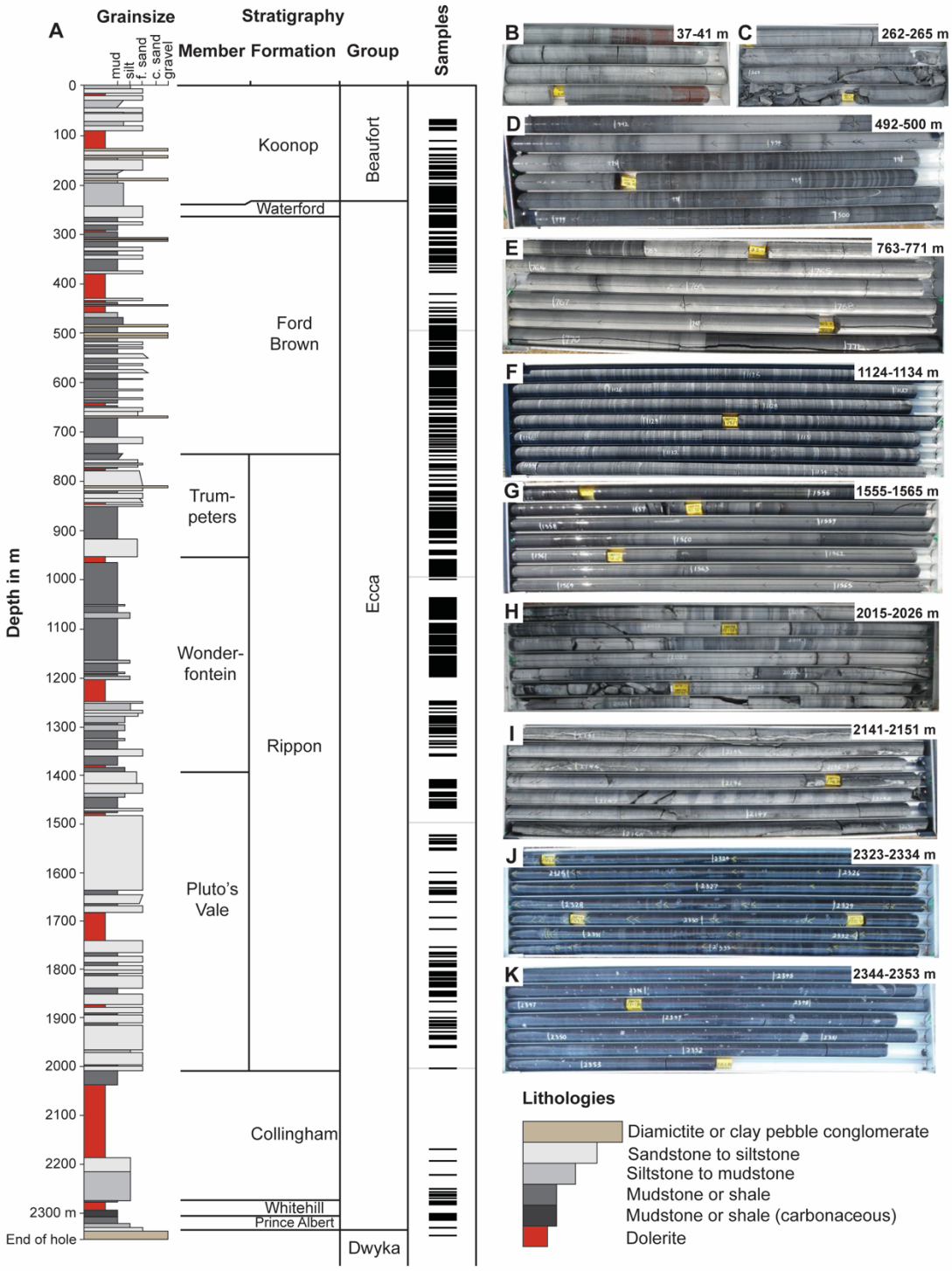

Figure 3. Simplified stratigraphic log of KWV-01 and sample positions (A). Representative photographs of core from the Koonop Formation (B), Waterford Formation (C), Fort Brown Formation (D), Trumpeters Member (E), Wonderfontein Member (F), Pluto's Vale Member (G), Collingham Formation (H), dolerite (I), Whitehill Formation (J), and the Dwyka Group (K). Note the reference line marking relative orientation and up direction on the core.

4. Results

4.1. Rock magnetic results

Nine of 14 samples acquire IRM linearly (on a log scale) from 20-30 mT to 300 mT, but only reach or approach saturation above 700 mT (Figure 4A). AF demagnetization of IRM define mean destructive fields of 61-69 mT, while H_{CR} values are typically 89-100 mT with R-ratios of 0.35-0.40 (after Cisowski, 1980). IRM is acquired more steeply from 20 mT to 100 mT in two samples (i.e., 475.14 and 2245.3), and saturation is reached at 200-400 mT (Figure 4B). These samples have low mean destructive fields, H_{CR} values and R-ratios. IRM is acquired non-linearly in three samples (i.e., 191.13, 916.45, and 996.51). The samples approach saturation at fields above 700 mT. Steeper acquisition is seen in 191.13 and 996.51 before 100 mT, followed by less steep acquisition that becomes steeper again after 300 mT. These samples have mean destructive fields of 36-48 mT, H_{RC} values of 48-60 mT, and R-ratios of 0.40-0.44 (Figure 4C). Sample 916.45 show shallower acquisition before 100 mT, after which acquisition becomes steeper. It has a mean destructive field of 121 mT, H_{RC} of 139 mT, and a R-ratio of 0.46 (Figure 4D).

IRM acquisition curve decomposition identifies six possible components. When fitting such models, a strategy was followed to keep components within a relatively constant coercivity range throughout the sample set. Each component is described by its median coercive field, dispersion parameter, relative proportion, and skewness (Supporting Information S1). Any specific sample require two, but more commonly three, and rarely four phases to match the IRM acquisition spectra. Generally, IRM acquisition is dominated by a medium coercivity or MC1 component (mean coercivity = 122 ± 27 mT; Figure 4E). Samples that reach saturation above 700 mT display small contributions of both low and high coercivity phases (LC1 with a mean coercivity of 26 ± 6 mT; and HC1 with a mean coercivity of 488 ± 51 mT) in addition to the main contribution of MC1, and in one case there is also a small contribution from a very high coercivity phase (i.e., HC2 with a mean coercivity of 1284 ± 401 mT). Samples that reach saturation at 200-400 mT display either low (i.e., LC2 with a mean coercivity of 51 ± 7 mT) or medium coercivity phases (i.e., MC1) as main contributors to the IRM together with a small contribution of LC1, but without higher coercivity phases contributing (Figure 4F). Non-linear IRM acquisition is characterized by either dominant LC2 contributions (in 191.13 and 996.51; Figure 4G) or by a dominant medium coercivity (i.e., MC2 with a mean coercivity of 274 ± 47 mT) in 916.45 (Figure

4H). There are additional small contributions of LC1 and MC2 phases in 191.13, and by MC2 and HC2 phases in 996.51. Apart from a dominant MC2 phase, a small LC1 contribution is also recognized in the IRM acquisition by sample 916.45.

An ARM version of the Lowrie-Fuller test (Johnson et al., 1975) shows harder AF demagnetization of ARM than that of the IRM for all specimens (Figure 5A), thus indicating the dominance of interacting single-domain (SD) particles. The ARM acquisition for all the specimens confirm high inter-particle interaction. Interaction is highest for 231.42, 425.45, and 475.14, which resemble ARM acquisition by chiton teeth. Curves otherwise resemble ARM acquisition by partially collapsed bacterial magnetosomes (Figure 5B). The least inter-particle interactions are seen in 2245.3, 996.51, 916.45, and 191.13.

Plots of NRM and ARM demagnetization values against IRM demagnetization for select specimens reveal a conspicuous soft NRM component in most specimens that is removed by 10 mT (Figure 5C). The ratio of NRM to IRMs is generally in the 1:1000 range for demagnetization between 10 mT and 50 mT for most specimens, but for four specimens (716.74, 916.45, 996.51, and 1764.7) the ratio was in the 1:100 range. At higher field levels the AF demagnetization of NRM proceed much slower than the AF demagnetization of IRM, and the curve is characteristically concave upwards for all our specimens. The ARM behaves similarly, albeit less pronounced. ARM:IRM values are above 0.1 in all specimens and are equal to, or exceed 1 at demagnetization levels above 70 mT (Figure 5C).

4.2. Demagnetization

4.2.1. Sedimentary rocks

Four magnetic components were identified during demagnetization of sedimentary rock specimens (Table 1). The demagnetization behaviour was variable as expected for the range of different lithologies and grain sizes. The four components were a low coercivity or soft magnetic component (SFT); a variable, but typically north to northwest directed and moderately steep upward directed component (A); a northerly and steep upward directed high stability magnetization (B-); and a southerly and steep downward directed high stability magnetization (B+). Any specific specimen, however, recorded a maximum of three components, and many were characterized by just two components or a single magnetic component (Figure 6 and 7).

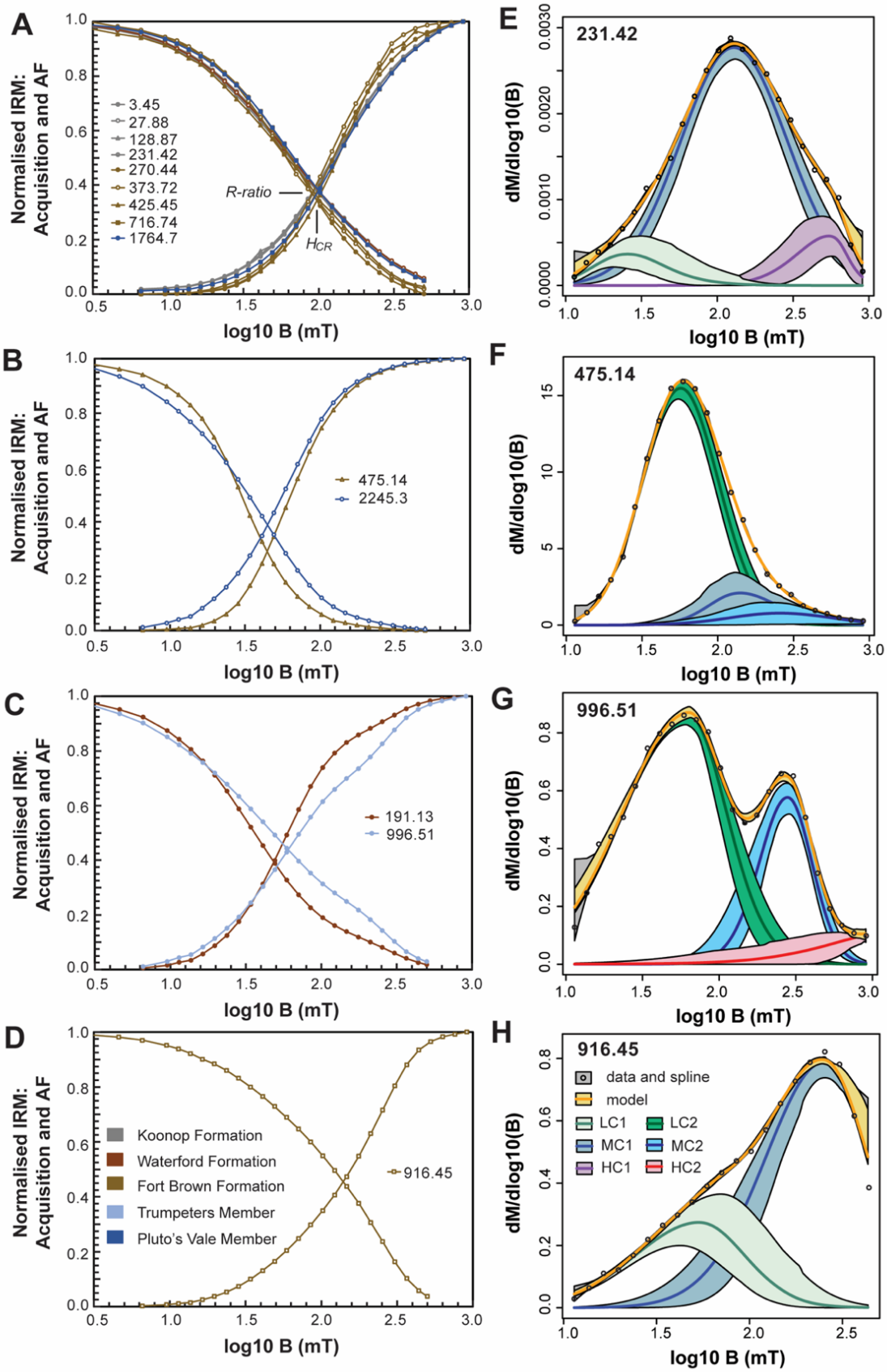

Figure 4. Acquisition and AF demagnetization of IRM of selected samples (A-D) and components of IRM identified through IRM acquisition curve decomposition (E-H).

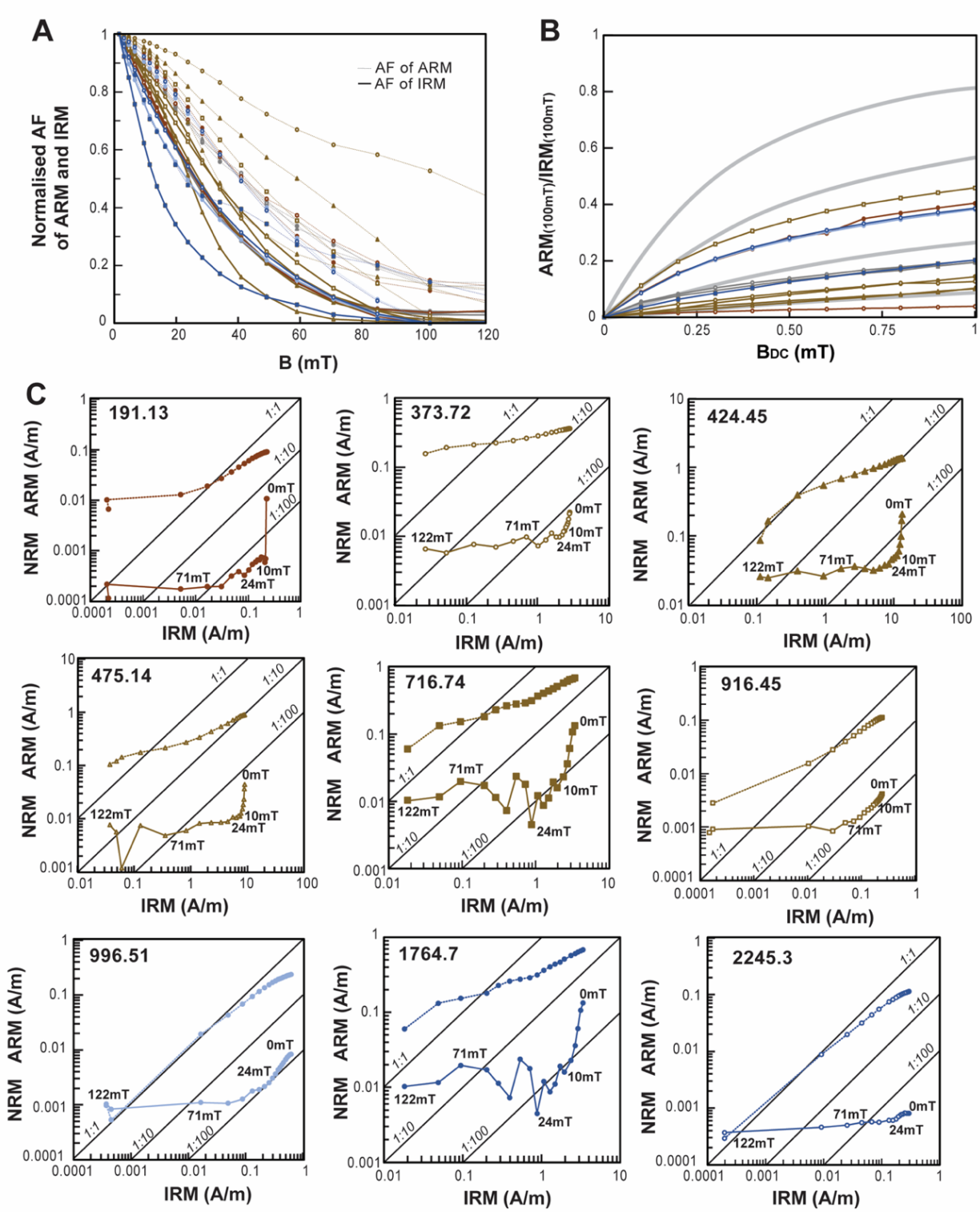

Figure 5. ARM version of the Lowrie-Fuller test for selected samples (A); ARM acquisition (B) for selected samples compared against intact magnetotactic bacteria (top grey line), partially collapsed bacterial magnetosomes (middle grey line), and chiton teeth (lower grey line); and plots of NRM and ARM demagnetization values against IRM demagnetization for selected samples (C). The lines in the background mark different ratios of NRM or ARM to IRM (i.e., 1:1, 1:10 or 1:100).

306 The demagnetization behaviour of nine specimens proved too erratic for the
307 identification of any magnetic components (Figure 6A), and these are not further
308 considered.
309 A low coercivity SFT components was identified in 220 of 400 specimens during
310 AF demagnetization steps up to low temperature demagnetization steps (Figure 6, 7
311 and 8). The SFT component is poorly defined in most with MAD values > 15° for fits
312 from 56 of the specimens. These components are randomly directed and not
313 considered to be of any geological significance.
314 After the removal of SFT components, prominent remanence components (i.e.,
315 component A) unblocked as either linear trajectories towards the origin or as linear
316 trajectories that clearly miss the origin to reveal the presence of remanence
317 components of higher thermal stability (Figure 6 and 7). These A components were
318 identified in 311 specimens (plus 34 specimens in which it was identified, but which
319 were excluded due to their > 15° MAD values). A components are highly variable in
320 terms of their unblocking and direction. They are generally northerly and upward
321 directed with a component average declination of 350.2°, inclination of -75.5° and α_{95}
322 of 3.74°, but with a very low precision parameter (k = 5.55) and a correspondingly
323 large standard deviation (Figure 9A). The A components either unblock by 340°C or
324 by 460°C in general.
325 In specimens where A component trajectories do not demagnetize towards the
326 origin, higher stability components (B- and B+) are revealed as either stable end-points
327 of demagnetization, linear demagnetization trajectories towards the origin, or more
328 commonly as demagnetizations as planes away from the A component direction
329 towards B+ component directions seen on equal area plots (Figure 6C-F and Figure
330 7E-F). The B- and B+ components variably unblock between 250°C and 520°C, a
331 rather wide range of thermal demagnetization steps, but most commonly unblock
332 above 400°C. B- components were identified in 65 specimens (plus 2 specimens in
333 which it was identified, but which were excluded due to their > 15° MAD values). The
334 B- components are northerly and upwards directed and often steeper than A
335 components. The component average was calculated at declination = 319.3°,
336 inclination = -73.6°, α_{95} = 5.86°, and k = 10.02 (Figure 9B). The distribution of B-
337 components is obviously elongated, but this is an artifact of imperfect orientation of
338 the drill core (see De Kock et al., 2009 for a description of this artifact). B+ components
339 were most commonly identified as demagnetization along planes away from the A

component direction (i.e., in 122 specimen after the exclusion of 10 specimen for which planes had MAD values that were > 20°), but also as components with linear demagnetization trajectories towards the origin after the removal of SFT and A components (i.e., in 37 specimens), and rarely (i.e., in 9 specimens) as single remanence components (Figure 7A-F). Considering only line data, a B+ component average is calculated at declination = 144.6°, inclination = 62.2°, α_{95} = 9.34°, and k = 6.05 (Figure 9C). Like the B- components, the B+ components also define an elongated distribution. Combining fitted lines and planes yield a B+ component average at declination = 153.5°, inclination = 65.3°, α_{95} = 3.88°, and k = 8.74 (Figure 9C). The B- and B+ components are near antipodal, but the line fit data fail to pass the reversal tests of McFadden and McElhinny (1990) with in-situ remanence directions. If the polarity of the B+ mean is reversed and compared to the B- mean it can be seen that the angle that separates the two means is 11.56°, which is larger than the critical angle of separation (10.44°) at which the two means would be statistically indistinguishable (i.e., 180° apart). Repeating the same test with tilt-corrected remanence directions, however, passes a C quality reversals test. The angle that separates the two means is 11.75°, which is smaller than the critical angle of separation of 14.36°. A combination of B- and B+ components (line fits only) yield an overall tilt-corrected mean at declination = 324.4°, inclination = -70.5°, α_{95} = 5.25°, and k = 7.50 for 111 specimens. Inclusion of plane fits yield an overall tilt-corrected mean at declination = 333.3°, inclination = -69.0°, α_{95} = 3.39°, and k = 8.31 for 235 specimens.

4.2.2. Dolerite

A 34.8 m-thick dolerite that intrudes the Koonap Formation between 127.11 and 92.24 m-depth. The magnetization of two specimens (i.e., KWV92.38 and KWV113.7) are characterized by small contributions of SFT components and dominated by northerly up directed magnetizations that remain stable above 400°C (i.e., DOL components; Figure 8). Sedimentary rock specimens above and below the dolerite are characterized by demagnetization along planes away from prominent A components (up) towards B+ components (down). The A components of specimens surrounding the intrusion is comparable to the DOL direction, and it appears that the magnetic effects of this intrusion on the surrounding sedimentary units was limited.

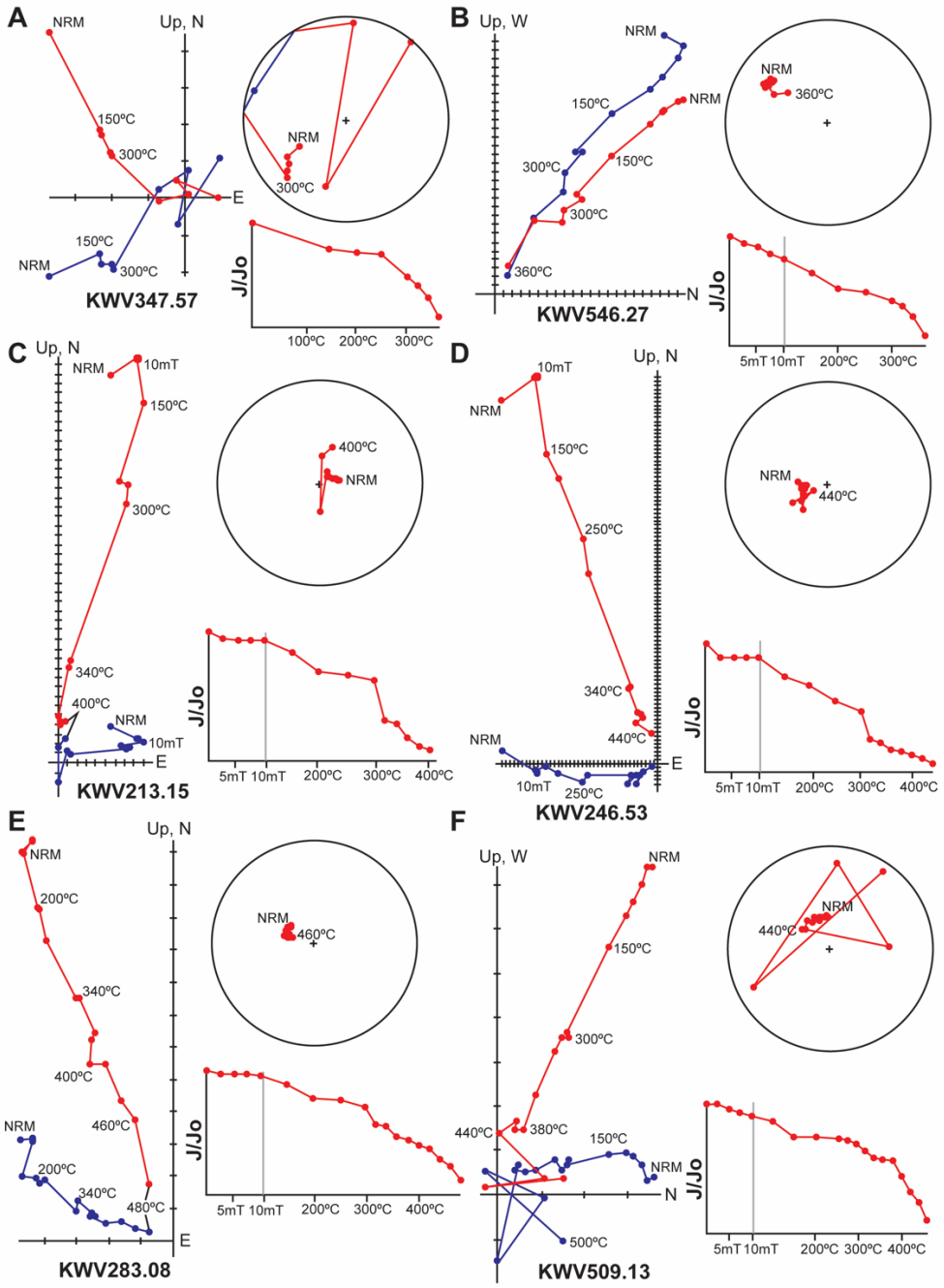

Figure 6. Representative demagnetization behaviour of selected specimens. A) KWV347.75 display an A component only (150°C to 300°C) before becoming erratic. B) KWV546.27 is dominated by an origin-seeking A component as a single magnetic component. C) KWV213.15, D) KWV246.53, E) KWV283.08 and F) KWV509.13 all display A components that miss the origin up to ~350°C before steeper origin-seeking trajectories define the B- components. KWV213.15 and KWV246.53 display small contributions of SFT components to the remanence that are removed by AF demagnetization steps. Zijderveld diagrams: red = inclination data, blue = declination data. Equal-area nets: red = up, blue = down. J/Jo = normalized magnetization.

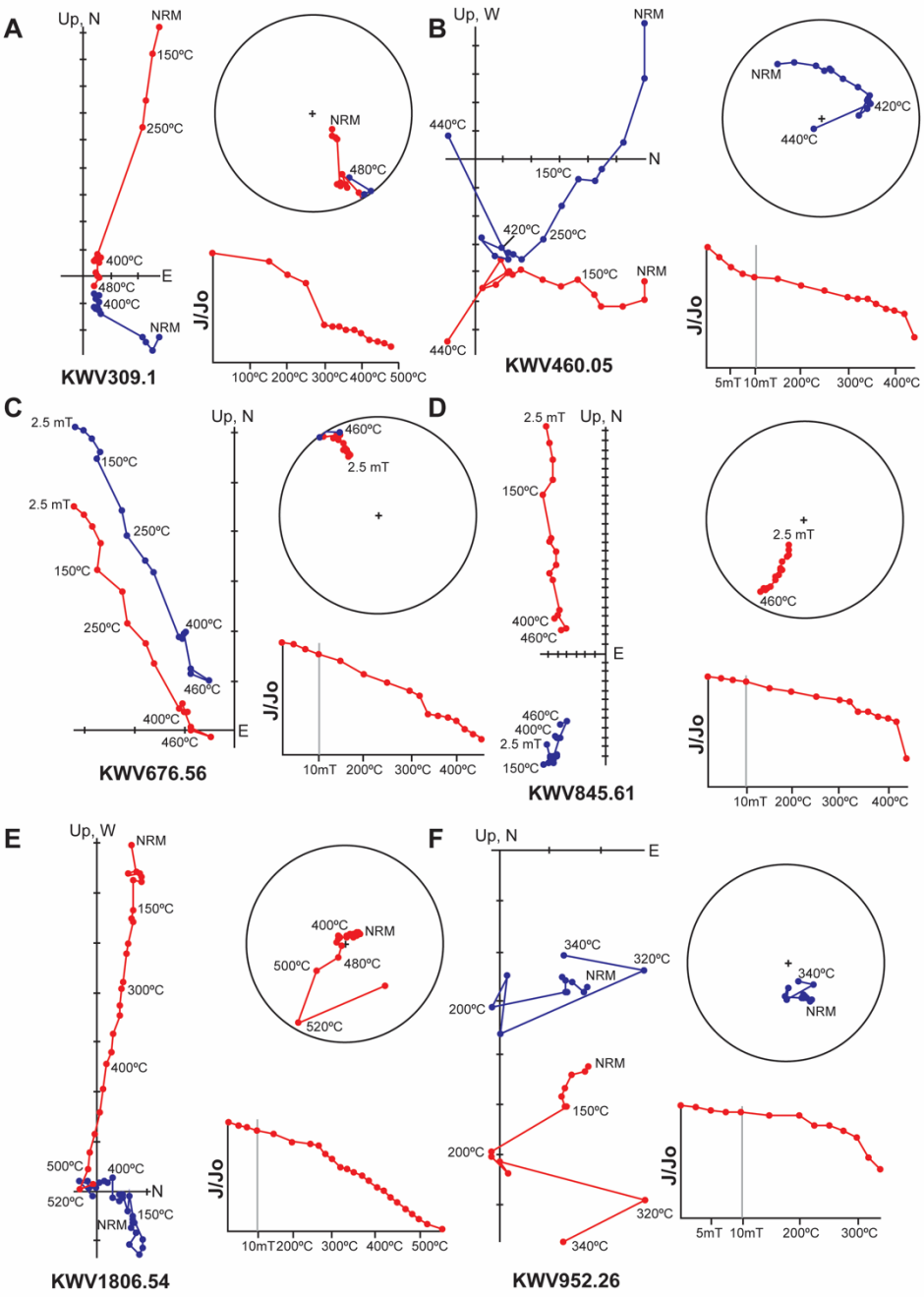

Figure 7. Representative demagnetization behaviour of selected specimens. A) KWV309.1, B) KWV460.05, C) KWV676.56, D) KWV845.61, and E) KWV1806.56 display small contributions of SFT components after which an A component unblocks as a linear trajectory that miss the origin. At high temperature demagnetization steps, component B+ is revealed as planes of demagnetization away from the A component direction to rarely reach stable end points of demagnetization (e.g., KWV460.05). F) In a few cases like KWV952.26, component B+ is the only remanence component that unblocks. Zijderveld diagrams: red = inclination data, blue = declination data. Equal-area nets: red = up, blue = down. J/Jo = normalized magnetization.

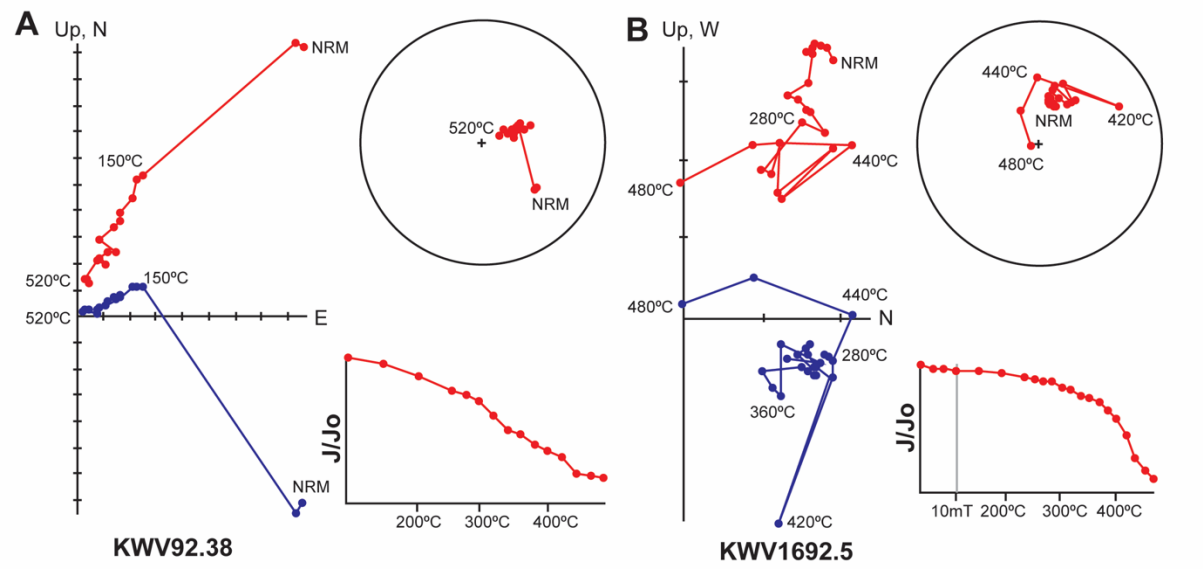

Figure 8. Representative demagnetization behaviour of selected dolerite specimens. A) KWV92.38, B) KWV1692.5 are dominated by northeast up DOL components. Either as origin seeking-trajectories (e.g., KWV92.38) or as stable endpoints of magnetization (e.g., KWV1692.5). Zijderveld diagrams: red = inclination data, blue = declination data. Equal-area nets: red = up, blue = down. J/Jo = normalized magnetization.

Several closely spaced dolerite intrusions with a cumulative thickness of 71.75 m intrude the upper part of the Fort Brown Formation between ~380 and ~460 m-depth. One specimen (i.e., KWV443.24) yielded a DOL component below 420°C, but another (i.e., KWV452.98) does not conform. It yielded a southwest and downward directed magnetization with a small SFT component contribution, but its demagnetization behaviour becomes increasingly erratic above 250°C. Sedimentary units up to 70m above the intrusion generally behaved erratically during demagnetization. One specimen from near the upper contact with the intrusion yielded a B+ component via a plane fit. Specimens from up to 50m below the intrusion yielded A components below ~300°C and B+ components constrained by line as well as plane fits above ~300°C . The contrast between these dolerite intrusions and the surrounding units is less clear.

Thin (< 5 m-thick) intrusions in the Trumpeters Member near 780 m-depth and 850 m-depth were not sampled. Sedimentary rock specimens around the intrusion at 780 m (i.e., KWV783.05KWV777.08) yield only north up (component A) with small SFT component contributions. Immediately above the intrusion at 850 m-depth specimen (KWV845.61) demagnetize away from a northerly up (component A) direction towards

418 a southerly down (component B+) direction. A specimen from immediately below the
419 intrusion (KWV853.18) record a single remanence component that is north-easterly
420 and up directed (component A).
421 A ~12 m-thick dolerite intrudes along with the contact between sandy units of the
422 Trumpeters Member and carbonaceous shale of the Wonderfontein Member around
423 960 m-depth. The dolerite was not sampled, but the sandy unit immediately above the
424 sill yielded well defined moderate to steep south-easterly down (B+) magnetizations
425 stable up to 460°C (i.e., KWV952.26 and KWV955.32). At lower thermal
426 demagnetization steps northerly up magnetizations (A components) were removed.
427 The Wonderfontein Member shale immediately below the sill also yielded well defined
428 moderate to steep south-easterly down (B+) magnetizations stable up to 460°C (i.e.,
429 KWV966.56) with a north up (A) component removed at lower thermal
430 demagnetization steps. The magnetic effect of this dolerite on the surrounding
431 sedimentary rocks seems to be minimal. Between 1200 to 1245 m-depth the
432 Wonderfontein Member is cut by ~45 m-thick coarse-grained dolerite. Two specimens
433 of dolerite near the top of this sill yielded northerly up magnetizations that were stable
434 up to ~300°C (DOL components), but with -17.9° the DOL component in specimen
435 KWV1203.66 was much lower inclined than the -44.4° of the DOL component in
436 KWV1200.86. Sedimentary specimen above the dolerite (KWV1197.87) yield
437 demagnetization trajectories towards a steep downward directed remanence (B+
438 component). Below the dolerite, sedimentary specimens also yield steep downward
439 directed directions. Neither sedimentary rocks associated with, nor a thin (< 5 m-thick)
440 dolerite near the base of the Wonderfontein Member around 1380 m-depth was
441 sampled.
442 A ~5 m-thick dolerite intrudes the upper Pluto's Vale Member around 1480 m-
443 depth. Neither this dolerite, nor sedimentary units in immediate association with it was
444 sampled. Multiple sills with a cumulative thickness of ~60 m intrude the upper Pluto's
445 Vale Member between 1680 and 1740 m-depth. Two dolerite specimens (KWV1692.5
446 and KWV1717.27) yielded north up DOL components that were stable up to 400°C
447 with minor contributions by SFT components. Sedimentary rock units immediately
448 above and below the intrusion displayed clear demagnetization trajectories along
449 planes away from the A components towards a B+ remanence.
450 A ~5m-thick dolerite intrusion between 1870 and 1880 m-depth was not sampled.
451 A very thick series of dolerite intrusions with a cumulative thickness of ~148 m is

present in the lower Pluto's Vale Member. One specimen (KWV2272.42) from these intrusions reveal a northwest up DOL component that remains stable up to 300°C. A second specimen (KWV2276.13) displayed erratic demagnetization behaviour and no fits were attempted. Sedimentary rock units above and below the dolerite are mainly characterized only by prominent A components. Only at 2251.11 m, some 20 m above the intrusions is a B+ remanence recorded. Below the intrusions, the closest specimen is at 2294.95 m, and it also record the B+ remanence.

A ~18 m-thick dolerite intrudes carbonaceous shale of the Whitehill Formation. This intrusion was not sampled, but sedimentary rock specimens above and below the dolerite (like the lowermost Pluto's Vale Member) at 2294.95 m and 2301.5 m record the B+ remanence.

An average for the northerly up DOL components was calculated from six specimens at declination = 57.3°, inclination = -68.8°, α_{95} = 24.04°, and k = 7.26 (Figure 9D).

5. Discussion

5.1. Carriers of remanence

NRM:IRM ratios in the 1:1000 range are consistent with the NRM largely being a post-depositional or depositional remanent magentization (pDRM or DRM), while those in the 1:100 range are more characteristic of secondary magnetizations, possibly a thermal remanent magnetization (TRM) due to the heating effects of dolerite intrusions, or a chemical remanent magnetization (CRM) due to diagenetic alteration in response to burial. The latter seems a less likely explanation, as there is no clear stratigraphic relationship with NRM:IRM ratios. The pronounced concave upward shape of the NRM:IRM curves suggest that magnetically soft phases (LC1 and LC2) are not efficient carriers of weak field remanent magnetization. Samples dominated by LC1 and LC2 phases reach saturation by 200 mT, suggesting these phases to be multi-domain low-Ti magnetite. NRM carried in high-coercivity phases are effectively immune to AF demagnetization and flattens out the NRM:IRM curves. The HC2 phase, which was only seen as a very minor contributor to IRM in three samples, is likely very fine-grained hematite. This phase is not an important carrier of remanence, because none of the specimens carried stable magnetizations after demagnetization above 540°C. HC1 is present in most samples as a minor contributor to IRM and could be pyrrhotite. Pyrrhotite has been identified in mudstones of the Whitehill and

Collingham formations in KWV by means of x-ray diffraction (Geel et al., 2021). Pyrrhotite may be responsible for the drops in magnetization seen during heating of specimens between 250°C and 300°C. The identities of the MC1 and MC2 phases, the main carriers of the NRM are less clearly diagnosed but are likely pseudo-SD or SD low-Ti magnetite phases, and together with the HC1 phase (i.e., pyrrhotite?) carriers of the A, B+ and B- components.

5.2. Timing of remanence acquisition and paleopole calculation

The DOL component seen in the KLIP intrusions is clearly different from the B+ magnetizations revealed during high temperature demagnetization steps in the surrounding sedimentary units. The DOL direction is comparable to the B- directions, although nowhere in direct association in the core. The DOL direction is also comparable to the lower temperature A direction that is developed throughout most of the core (Figure 6; Table 1). The DOL direction is, however, statistically distinguishable from the B- component. The separation angle between the means is 28.3° and larger than the critical angle of 20.7° at which the two means would be indistinguishable. A direct comparison of the DOL and A directions shows that they are statistically the same. The separation angle between the means is 20.1° and smaller than the critical angle of 26.3° at which the two means would be indistinguishable. We therefore interpret the A component as a younger remanence that was acquired during the intrusion of the KLIP dolerites. The B+ and B- components are interpreted to be older magnetizations, and likely primary Permian magnetizations recorded as pDRMs or DRMs that pass a quality C reversals test for tilt-corrected remanence directions. Paleopoles were calculated for the DOL and A components based on in-situ remanence directions, and for the B+ and B- components based on remanence directions after bedding was restored to paleohorizontal.

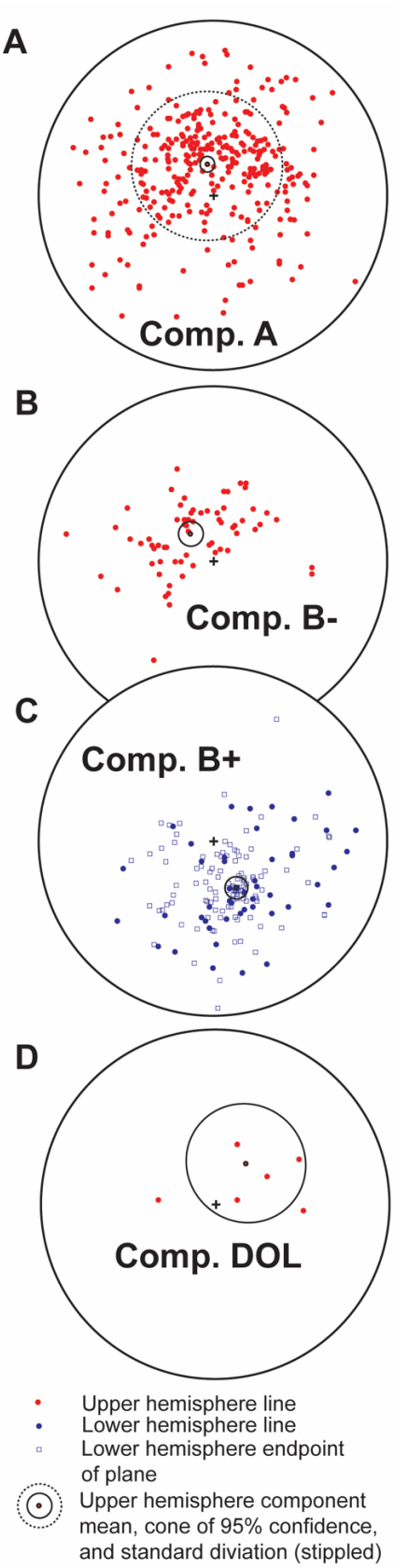

Figure 9. Identified magnetic components and their means. A) Component A, B) Component B-, C) Component B+, and D) Component DOL. All diagrams are of in-situ remanence directions.

B-, B+ and their combined paleopoles are comparable to the 240 Ma to 180 Ma segment of the Gondwana reference apparent polar wander path of Torsvik et al. (2012). We follow Torsvik et al. (2012) by applying a correction for inferred inclination shallowing for detrital sediments of f = 0.6, where:

tan(observed inclination) = f tan (corrected inclination)

Such a correction yield B-, B+ and combined paleopoles that are comparable to the 280 Ma to 210 Ma segment of the Gondwana reference apparent polar wander path (Figure 10). Our inclination corrected pole is also comparable to the Ecca Group pole presented for the KZF-01 core from the southwestern Karoo basin of Abubakre and De Kock (2021) as well as the lower Beaufort Group poles of Lanci et al. (2013) and Tohver et al. (2015) (Figure 10). However, our pole is distinct form the Ecca Group pole of Belica et al. (2017a), which plots further to the east from our pole as well as the 280-240 Ma segment of the Gondwana reference apparent polar wander path of Torsvik et al. (2012) (Figure 10).

Table 1: Summary of remanence components identified in KWV-01 and their corresponding paleopoles

Com-ponent	n	In-situ remanence				Tilt-corrected remanence*				Paleopole		
		Decl. in °	Incl. in °	k	α_{95} in °	Decl. in °	Incl. in ° (f=0.6)	k	α_{95} in °	Plat in °N (f=0.6)	Plong in °E (f=0.6)	dp/dm in ° (f=0.6)
DOL	6	57.3	-68.8	7.26	24.04	58.6	-72.4	5.97	26.88	-44.6	342.2	34.5/40.7
A	311	350.2	-75.5	5.55	3.74	354.1	-76.2	5.26	3.86	-58.9	36.5	6.3/6.9
B-	65	319.3	-73.6	10.02	5.86	322.8	-75.2 (-81.0)	8.84	6.28	-51.9 (-45.4)	55.8 (43.7)	10.5/11.5 (11.7/12.1)
B+ (lines only)	46	144.6	62.2	6.05	9.34	145.7	63.5 (73.4)	6.49	8.96	-60.6 (-54.7)	82.7 (58.5)	11.2/14.2 (14.4/16.1)
B+ (lines and planes)	170	153.5	65.3	8.74	3.88	155.8	66.5 (75.4)	8.32	3.99	-65.3 (-56.1)	68.7 (48.4)	5.4/6.6 (6.7/7.3)
B+/- (lines only)	111	322.1	-69.1	7.70	5.18	324.4	-70.5 (-78.0)	7.50	5.25	-56.4 (-49.5)	66.0 (49.1)	7.9/9.1 (9.3/9.9)
B+/- (lines and planes)	235	150.6	67.7	8.89	3.27	153.3	69.0 (77.0)	8.31	3.39	-62.0 (-53.2)	64.3 (46.9)	4.9/5.8 (5.9/6.3)

*Structural correction applied to restore bedding as per electrical dip meter log.
Abbreviations: n = number of specimens, Decl. = declination, Incl. = inclination, k = precision parameter, α_{95} = radius of the cone of 95% confidence around the mean, Plat = VGP latitude, Plong = VGP longitude, dp/dm = semi-minor/semi-major axes of oval of 95% confidence around the calculated pole, "f = 0.6" indicates inclination corrected for shallowing and corresponding paleopoles calculated from these corrected values.

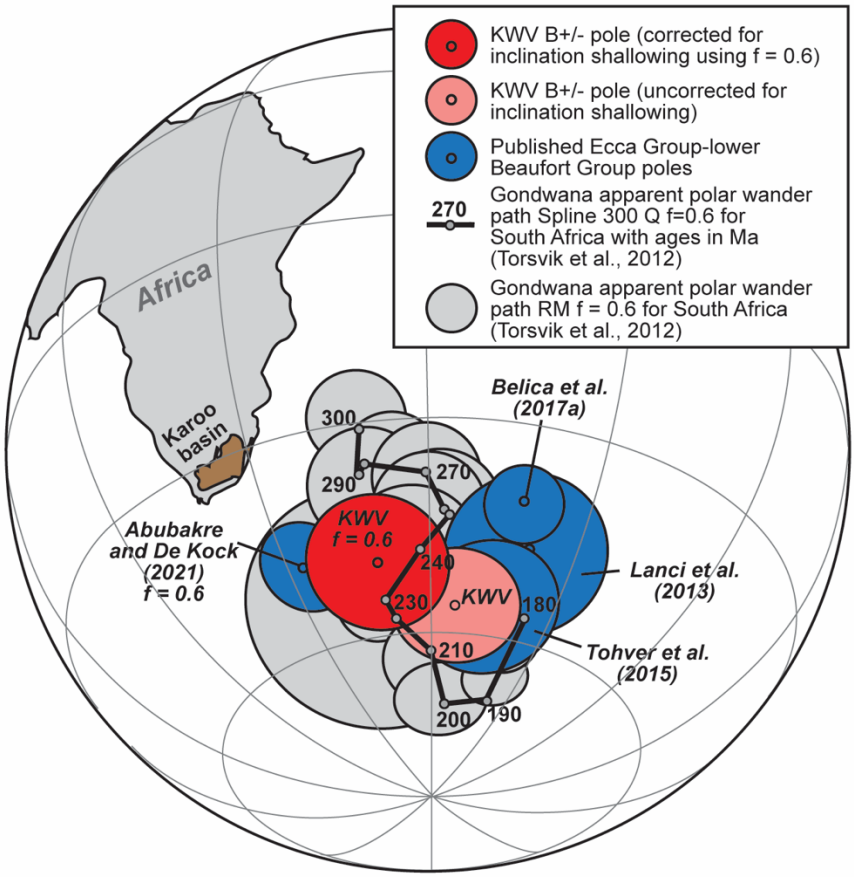

Figure 10. The Ecca Group-lower Beaufort Group B+/- pole from KWV-01 (uncorrected and corrected for inclination shallowing) compared to published poles and the Gondwana apparent polar wander path of Torsvik et al. (2012) in South African coordinates.

5.3. Magnetostratigraphy and end of the Kiaman Reverse Polarity Superchron in KWV-01

The B- and B+ remanence directions define stratigraphically bound groupings and can be used to construct a magnetostratigraphy for KWV-01 (Figure 11). The core is dominated by reverse polarity zones, with three normal polarity zones are recorded in KWV-01 and are labelled KWV2n, KWV3n and KWV4n. Normal polarity zone KWV4n is recorded in the uppermost specimens of the core and within the Koonop Formation. The remainder of the Koonop Formation, Waterford Formation and the uppermost Fort Brown Formation define polarity chron KWV3 between 325 m and 20 m depth. It is defined by a prominent normal polarity zone (137 m to 328 m) and reverse polarity zone (20 m to 137 m) with possible normal polarity subzones at 82 m depth, and

562 several possible reverse polarity subzones within KWV3n. The presence of a normal
563 magnetized dolerite sill within the Koonop Formation does not affect resolution of the
564 KWV3r polarity zone. The Fort Brown Formation host one magnetic polarity chron (i.e.,
565 KWV2). The KWV2r reverse polarity zone is well defined between 328 m and 446 m,
566 but normal polarity zone KWV2n is perhaps partially obscured by the effects of a
567 possible reversely magnetized thin dolerite sill (Figure 11). KWV2n does appear to
568 extend to 522 m. The remainder of the core is dominated by a very thick reverse
569 polarity zone (KWV1r), but four well defined normal polarity subzones are recorded in
570 the lower Fort Brown Formation (i.e., KWV1r.2n, KWV1r.3n, and KWV1r.4n) and the
571 middle of the Trumpeters Member (i.e., KWV1r.1n). Possible, but poorly defined
572 normal polarity subzones were identified within the Fort Brown Formation between
573 KWV1r.3n and KWV1r.4n at 600 m and within the Trumperts Member between
574 KWV1r.1n and KWV1r.2n at 781.5 m. Additional poorly defined normal polarity
575 subzones occur in the Wonderfontein Member (at 981 m and 1141 m), the Pluto's Vale
576 Member (at 1784 m), and at the base of the Collingham Formation (at 2259 m). Normal
577 magnetized dolerite intrusions within the Wonderfontein Member, the Pluto's Vale
578 Member, the Collingham Formation, and the Whitehill Formation appears to have little
579 effect on the resolution of the KVWr1 reverse polarity zone, except for the possible
580 normal polarity subzone at 2259 m. It cannot be ruled out that this specimen's
581 magnetization is overprinted by the intrusion within the Whitehill Formation. It should
582 also be noted that sample coverage between 1923 m and 2200 m is poor. Although
583 this interval is largely represented by dolerite, the polarity interpretation for
584 sedimentary units in the interval is regarded as uncertain (Figure 11).
585

586 **5.4. Magnetostratigraphic correlation and geochronology of the Ecca Group**
587 **across the southern Karoo basin**
588

589 The magnetostratigraphy of KWV-01 can be correlated to that of southwestern Karoo
590 basin. In doing so, the KWV3n normal polarity zone in the upper Fort-Brown to lower
591 Koonop formations and the KWV4n normal polarity zone in the Koonop Formation can
592 be correlated to the N2 normal polarity zones identified by Lanci et al. (2013) within
593 the Abrahamskraal Formation at Ouberg Pass (Figure 12). The thin KWV2n normal
594 polarity zone in the middle of the Fort Brown Formation would then correlate to N3
595 identified by Lanci et al. (2013) in the Waterford Formation (Figure 12). Correlation of

normal polarity sub zones (i.e., KWV1r.4n, KWV1r, 3n, KWV1r.2n, and KWV1r.1n) are less obvious, but we suggest a correlation of the normal polarity zone within the Tierberg Formation (Abubakre and De Kock, 2021) at the top of borehole KZF-01 to KWV1r.1n (Figure 12). Two normal polarity zones at the top of the Collingham Formation and base of the Price Albert Formation in KZF-01 (Abubakre and De Kock, 2021) are not clearly identified in KWV-01.

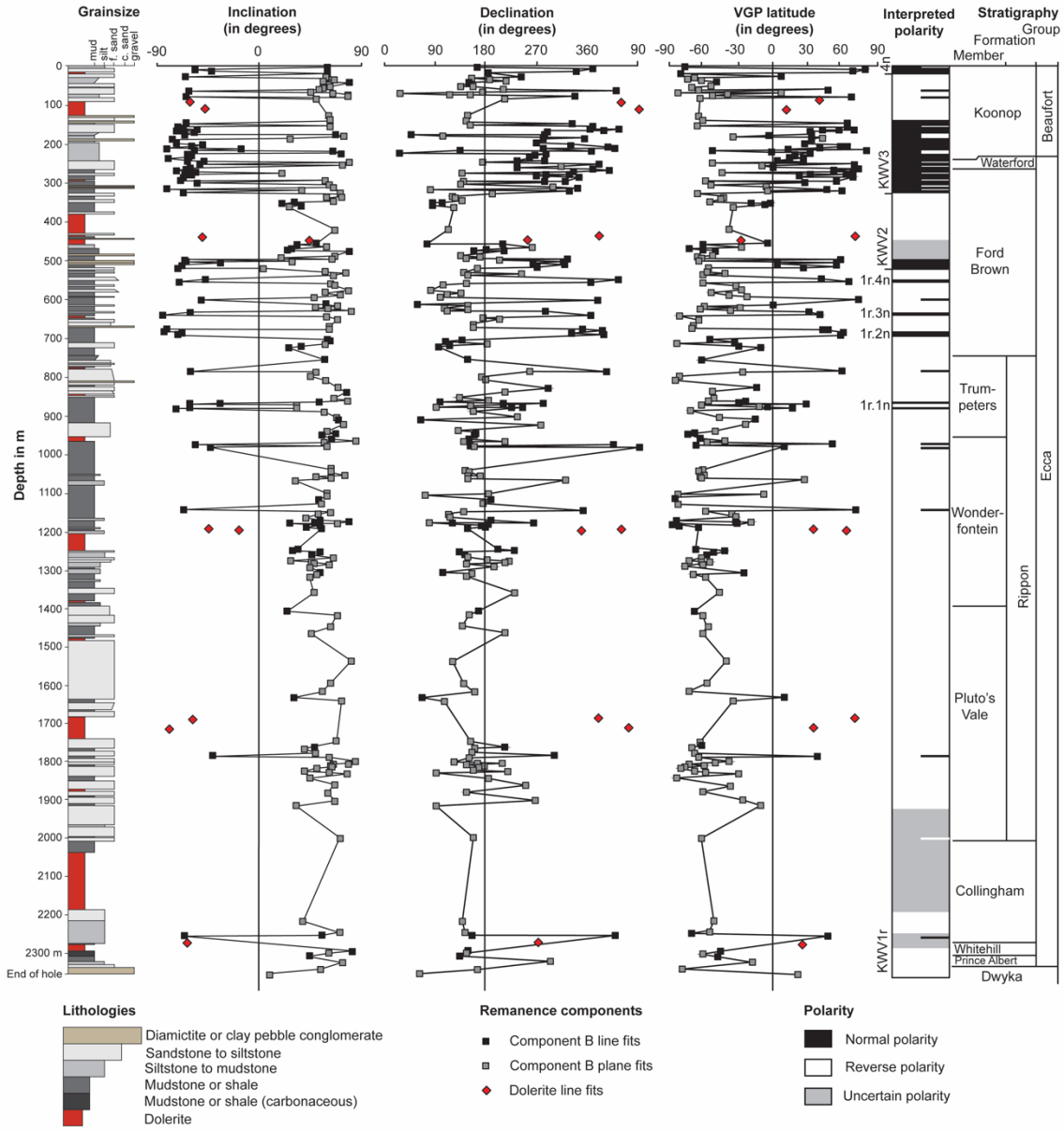

Figure 11. Magnetic polarity interpretation for KWV-01 based on inclination, declination, and VGP latitude stratigraphic variation of the B- and B+ remanence directions (All indicated here as in-situ remanence directions). Magnetic components identified in dolerite intrusions are illustrated for comparison.

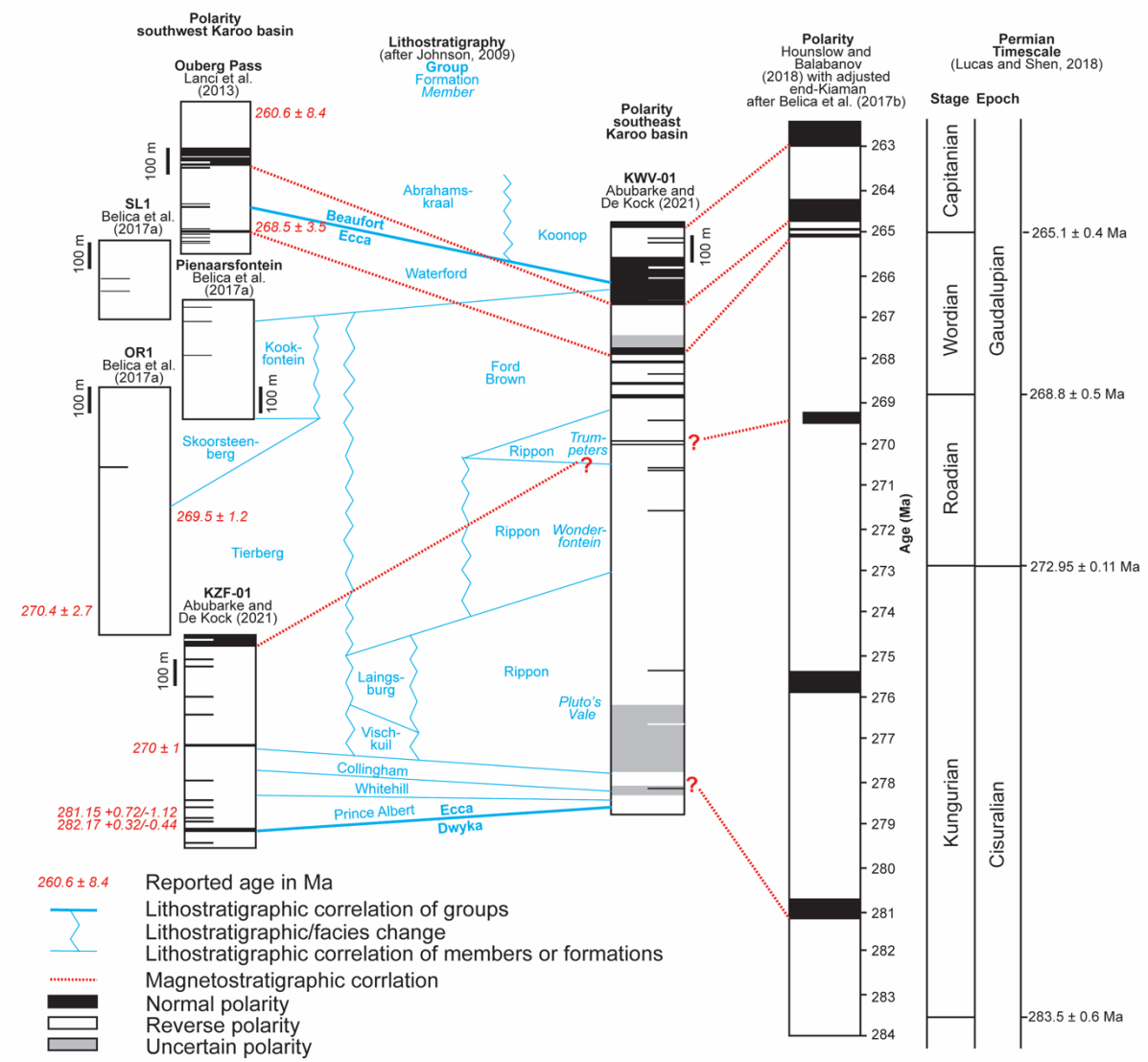

Figure 12. Magnetostratigraphic and lithostratigraphic correlation between the southwest and southeast Karoo basin and the Permian composite reference magnetostratigraphic record. See the text for details on the reported ages from the southwest Karoo basin.

The normal polarity zones at the top of KWV-01 are interpreted to mark the onset of the Illawara mixed polarity zone at the top of the Kiaman Normal Polarity Superchron. The end of the Kiaman Normal Polarity Superchron is placed at or near the base of the Capitanian, but the precise age was not well constrained (Hounslow and Balabanov, 2018; Menning et al., 2006; Steiner, 2006). Recently Belica et al. (2017b) constrained the end of the Kiaman Normal Polarity Superchron (i.e., the so-called Illawara reversal) to be between 265.05 ± 0.35 Ma (Ar-Ar on plagioclase) and a 263.51 ± 0.05 Ma (U-Pb thermal ionization mass spectrometry or TIMS age by Metcalfe et

al., 2015). Lanci et al. (2013) reported U-Pb sensitive high-resolution ion microprobe or SHRIMP zircon ages from tuffaceous units at Ouberg Pass within the Illawara mixed polarity zone of between 264-268 Ma, while McKay et al. (2015) reported a U-Pb SHRIMP zircon ages of 260.6 ± 8.9 Ma 264.7 ± 2.5 Ma from the Abrahamskraal Formation. Lanci et al. (2013) deduced a ~269 Ma age for the end of the Kiaman Normal Polarity Superchron. The relative imprecision of the SHRIMP ages, however, does not exclude an interpretation that places the Illawara reversal at ~265 Ma. The Tierberg, Kookfontein and much of the Waterford formations of the Ecca Group in the southwestern part of the basin is characterized by dominantly reversed magnetic polarity, with a normal polarity zone in the middle of the Tierberg Formation reported from the top of KWZ-01 and several poorly constrained normal polarity subzones in the Kookfontein, Skoorsteenberg and lower Tierberg formations (Abubakre and De Kock, 2021; Belica et al., 2017a). Belica et al. (2017a) correlated poorly characterized normal polarity subzones from OR1 and Pienaarsfontein to Kungurian normal polarity zones of the Geomagnetic Polarity Time Scale. Such a correlation is, however, not compatible with U-Pb SHRIMP zircon ages of 269.5 ± 1.2 Ma and 270.4 ± 2.7 Ma reported by Belica et al. (2017a) and McKay et al. (2016) from the Tierberg Formation. Here we suggest correlation of the normal polarity zone in the middle of the Tierberg Formation of Abubakre and De Kock (2021) to the late Roadian normal polarity zone in the reference composite of Hounslow and Balabanov (2018), which would account for the reported U-Pb SHRIMP zircon ages. In KWV-01, this can possibly be correlated to normal polarity subzone KWV1r.1n in the Trumpeters Member of the Rippon Formation (Figure 12). The deposition of the Prince Albert, Whitehill and Collingham formations are constrained between ~282 Ma to ~270 Ma by U-Pb SHRIMP zircon ages from tuffaceous units in the southwestern part of the basin (Griffis et al., 2019; Turner, 1999). Abubakre and De Kock (2021) thus correlated two short normal polarity subzones in KZF-01 to Kungurian normal polarity zones in the reference composite of Hounslow and Balabanov (2018). Normal polarity zones or subzones are not defined in KWV-01, but a possible normal polarity subzone (represented only by one specimen, and possibly affected by a nearby dolerite intrusion) in the Collingham Formation could be Kungurian in age.

The top of KWV-01 in the Koonop Formation can be constrained to be near 263 Ma, while the top of the Ecca Group in KWV-01 is well constrained as being deposited

655 during an early Capitanian normal polarity zone between 264 Ma and 265 Ma while
656 deposition of the Ecca Group likely commenced around ~281 Ma (Figure 12). As such
657 the KWV-01 span 18 million years of deposition of which the Ecca Group represents
658 ~16 million years. From the magnetostratigraphic correlation the lithostratigraphic
659 boundary between the Ecca Group and the Beaufort Group is shown to be time
660 transgressive. The boundary represents a change from marine to terrestrial facies and
661 has long been interpreted as diachronous and to young from the southwest to the
662 north based on sedimentology and biostratigraphy (Catuneanu et al., 2002; Rubidge,
663 2005; Rubidge et al., 1999). Here the position of the boundary is calibrated at near
664 265 Ma in the southwest at Ouberg Pass and closer to 264.5 Ma in the southeast in
665 KWV-01.
666

667 ## 6. Conclusions

668 The Permian rocks of the southeast Karoo basin in KWV-01 revealed dual polarity
669 primary remanence components (components B- and B+) that pass a quality C
670 reversals test as well as baked contact tests, where the rocks are in contact with
671 younger dolerite intrusions of the KLIP. These intrusions have affected much KWV-01
672 magnetically, and likely caused widespread acquisition of a lower stability northerly up
673 remanence (component A), which is indistinguishable from magnetizations recorded
674 by dolerite specimens (i.e., component DOL). The combined B+/- paleomagnetic pole
675 compares favourably with previously published paleopoles from the Ecca Group and
676 lower Beaufort Group. Sedimentary rocks in KWV-01 recorded predominantly B+
677 magnetizations representing the Kiaman Reverse Polarity Superchron. B-
678 magnetizations in KWV-01 define three normal polarity zones in the lower Koonop,
679 Waterford, and Ford Brown formations representing the Illawara mixed polarity zone.
680 As such, the end of the Kiaman Reverse Polarity Superchron is recorded in KWV-01
681 and can be correlated to southwestern part of the basin, where it is recorded at Ouberg
682 Pass. Correlation to the Permian reference composite magentostratigraphy suggest
683 an age of 264.5 Ma for the boundary between the Ecca and the Beaufort groups in
684 KWV-01, and ~265 Ma at Ouberg Pass, thus calibrating this diachronous boundary in
685 the southern Karoo basin for the first time.
686

687 ## 7. Acknowledgements

The authors acknowledge support from the South African Department of Science and Innovation and National Research Foundation Centre of Excellence for Integrated Mineral and Energy Resource Analysis (DSI-NRF CIMERA) through the Karoo Research Initiative (KARIN) project. Opinions expressed and conclusions arrived at are those of the authors, and not necessarily to be attributed to the Centre of Excellence. We thank J.L. Kirschvink for the use of the palaeomagnetism and rock magnetism laboratory at Caltech.

8. Data Availability Statement

The electrical dip meter log for KWV-01, details of core orientation, all demagnetization data, least squares fits as well as rock magnetic data used to create this manuscript are available at http://dx.doi.org/10.17632/f7p753f2hp.1. Least-squares analysis of demagnetization data, orthogonal diagrams, equal area nets and J/Jo diagrams were made using PaleoMag 3.2 (Jones, 2002), available at http://cires1.colorado.edu/people/jones.craig/PMag3.html. Paleopoles were visualized using GPlates 2.2 (Williams et al., 2012), available at https://www.gplates.org/. IRM acquisition curves were unmixed using the MAX Unmix software (Maxbauer et al., 2016) through the online application available at http://shinyapps.its.carleton.edu/max-unmix/.

9. References

Abubakre, A. O., and De Kock, M. O., 2021, Magnetostratigraphic constraints for early Permian rocks of the southwestern Karoo Basin, South Africa: Gondwana Research, v. 90, p. 220-240.

Bangert, B., Stollhofen, H., Lorenz, V., and Armstrong, R. A., 1999, The geochronology and significance of ash-fall tuffs in the glaciogenic Carboniferous-Permian Dwyka Group of Namibia and South Africa: Journal of African Earth Sciences, v. 29, no. 1, p. 33-49.

Belica, M. E., Tohver, E., Flint, S., Parra-Avila, L., Hodgson, D., Lanci, L., and Pisarevsky, S., 2017a, Refining the chronostratigraphy of the Karoo Basin, South Africa: magneostratigraphic constraints support an Early Permian age for the Ecca Group: Geophysical Journal International, v. 211, no. 3, p. 1354-1374.

Belica, M. E., Tohver, E., Pisarevsky, S. A., Jourdan, F., Denyszyn, S. W., and George, A. D., 2017b, Middle Permian paleomagnetism of the Sydney Basin, Eastern Gondwana: Testing Pangea models and the timing of the end of the Kiaman Reverse Superchron.: Tectonophysics, v. 699, no. 178-198.

Bordy, E. M., Hancox, P. J., and Rubidge, B. S., 2004, Basin development during the deposition of the Elliot Formation (Late Triassic - Early Jurassic) Karoo Supergroup, South Africa: South African Journal of Geology, v. 107, p. 397-412.

Butler, R. F., 1992, Paleomagnetism: magnetic domains to geologic terranes., Boston, Blackwell Scientific Publishers, 319 p.:

Catuneanu, O., Hancox, P. J., Cairncross, B., and Rubidge, B. S., 2002, Foredeep submarine fans and forebulde deltas: orogenic off-loading in the underfilled Kroo Basin: Journal of African Earth Sciences, v. 35, no. 489-502.

Cole, D. I., 1992, Evolution and development of the Karoo Basin, *in* De Wit, M. J., and Ransome, I. G. D., eds., Inversion tectonics of the Cape Fold Belt, Karoo and Cretaceous basins of southern Africa: Rotterdam, A.A. Balkema, p. 87-99.

Cortrell, R. D., Tarduno, J. A., and Roberts, J., 2008, The Kiaman Reversed Polarity Superchron at Kiama: Towards a field strength estimate based on single silicate crystals.: Physics of the Earth and Planetary Interiors, v. 169, no. 1, p. 49-58.

Council for Geoscience, 1997, Geological Map of the Republic of South Africa and the Kingdoms of Leshoto and Swaziland Council for Geoscience, scale 1:1 000 000.

De Kock, M. O., Evans, D. A. D., Kirschvink, J. L., Beukes, N. J., Rose, E., and Hilburn, I., 2009, Paleomagnetism of a Neoarchean-Paleoproterozoic carbonate ramp and carbonate platform succession (Transvaal Supergroup) from surface outcrop and drill core, Griqualand West region, South Africa.: Precambrian Research, v. 169, p. 80-99.

Fildani, A., Drinkwater, N. J., Weislogel, A., McHargue, T., Hodgson, D. M., and Flint, S. S., 2007, Age Controls on the Tanqua and Laingsburg Deep-Water Systems: New Insights on the Evolution and Sedimentary Fill of the Karoo Basin, South Africa: Journal of Sedimentary Research, v. 77, no. 11, p. 901-908.

Fildani, A., Weislogel, A., Drinkwater, N. J., McHargue, T., Tankard, A., Wooden, J., Hodgson, D., and Flint, S., 2009, U-Pb zircon ages from the southwestern Karoo Basin, South Africa--Implications for the Permian-Triassic boundary: Geology, v. 37, no. 8, p. 719-722.

Geel, C., Nolte, S., and Bordy, E. M., 2021, Geomechanical properties of the Permian black shales in the southern main Karoo Basin: lessons from compositional and petrophysical studies: South African Journal of Geology, v. 124, no. 3, p. 735-750.

Griffis, N. P., Montañez, I. P., Mundil, R., Richey, J., Isbell, J., Fedorchuk, N., Linol, B., Iannuzzi, R., Vesely, F., Mottin, T., da Rosa, E., Keller, B., and Yin, Q.-Z., 2019, Coupled stratigraphic and U-Pb zircon age constraints on the late Paleozoic icehouse-to-greenhouse turnover in south-central Gondwana: Geology, v. 47, no. 12, p. 1146-1150.

Hastie, W. W., Watkeys, M. K., and Aubourg, C., 2014, Magma flow in dyke swarms of the Karoo LIP: Implications for the mantle plume hypothesis: Gondwana Research, v. 25, no. 2, p. 736-755.

Hounslow, M. W., and Balabanov, Y. P., 2018, A geomagnetic polarity timescale for the Permian, calibrated to stage boundaries: Geological Society, London, Special Publications, v. 450, p. 61-103.

Hounslow, M. W., McIntosh, G., Edwards, R. A., Laming, D. J. C., and Karloukovski, V., 2016, End of the Kiaman Superchron in the Permian of SW England: magnetostratography of the Aylesbeare Mudstone and Exeter groups: Journal of the Geological Society, v. 174, p. 56-74.

Irving, E., 1963, Paleomagnetism of the Narrabeen Chocolate shales and the Tasmanian dolerite: Journal of Geophysical Research, v. 68, no. 8, p. 2283-2287.

Irving, E., and Parry, L., 1963, The magnetism of soem Permian rocks from New South Wales: Geophysical Journal International, v. 7, no. 4, p. 395-411.

773 Johnson, M. R., 2009, Ecca Group, *in* Johnson, M. R., ed., Catalogue of South African
774 lithostratigraphic units, Volume 10: Pretoria, SA Committee for Stratigraphy, p. 5-7.
775 Johnson, M. R., Van Vuuren, C. J., Hegenberger, W. F., Key, R., and Shoko, U., 1996,
776 Stratigraphy of the Karoo Supergroup in southern Africa: an overview: Journal of
777 African Earth Sciences, v. 23, no. 1, p. 3-15.
778 Johnson, M. R., Van Vuuren, C. J., Visser, J. N. J., Cole, D. I., Wickens, H. D., Christie, A. D. M.,
779 Roberts, D. L., and Brandl, G., 2006, Sedimentary rocks of the Karoo Supergroup., *in*
780 Johnson, M. R., Anhaeusser, C., and Thomas, R. J., eds., The Geology of South Africa.,
781 Geological Society of South Africa and Council for Geoscience, p. 461-499.
782 Jones, C. H., 2002, User-driven integrated software lives: "Paleomag" Paleomagnetic
783 analysis on the Macintosh TM.: Computers and Geosciences, v. 28, p. 1145-1151.
784 Jourdan, F., Féraud, G., Bertrand, H., Kampunzu, A. B., Tshoso, G., Watkeys, M. K., and Le
785 Gall, B., 2005, Karoo large igneous province: Brevity, origin, and relation to mass
786 extinction questioned by new 40Ar/39Ar age data: Geology, v. 33, no. 9, p. 745.
787 Kirschvink, J. L., 1980, The least-squares line and plane and the analysis of palaeomagnetic
788 data: Geophysical Journal of the Royal Astronomical Society, v. 62, p. 699-718.
789 Kirschvink, J. L., Isozaki, Y., Shibuya, H., O'tafuji, Y., Raub, T. D., Hilburn, I. A., Kasuya, T.,
790 Yokoyama, M., and Bonifacie, M., 2015, Challenging the sensitivity limits of
791 Paleomagnetism: Magnetostratigraphy of weakly magnetized Gaudalupian-Lopingian
792 (Permian) limestone from Kyushu, Japan: Palaeogeography, Palaeoclimatology,
793 Palaeoecology, v. 418, p. 75-89.
794 Lanci, L., Tohver, E., Wilson, A., and Flint, S., 2013, Upper Permian magnetic stratigraphy of
795 the lower Beaufort Group, Karoo Basin: Earth and Planetary Science Letters, v. 375,
796 p. 123-134.
797 Maxbauer, D. P., Feinberg, J. W., and Fox, D. L., 2016, MAX UnMix: A web application for
798 unmixing magnetic coercivity distributions.: Computers & Geosciences, v. 95, p. 140-
799 145.
800 McFadden, P. L., and McElhinny, M. W., 1988, The combined analysis of remagnetization
801 circles and direct observations in paleomagnetism: Earth and Planetary Science
802 Letters, v. 87, no. 1, p. 161-172.
803 McFadden, P. L., and McElhinny, M. W., 1990, Classification of the reversal test in
804 palaeomagnetism: Geophysical Journal International, v. 103, p. 725-729.
805 McKay, M. P., Coble, M. A., Hessler, A. M., Weislogel, A. L., and Fildani, A., 2016,
806 Petrogenesis and provenance of distal volcanic tuffs from Permian-Triassic Karoo
807 Basin, South Africa: A window into a dissected magmatic province: Geosphere, v. 12,
808 no. 1, p. 1-14.
809 McKay, M. P., Weislogel, A. L., Fildani, A., Brunt, R. L., Hodgson, D. M., and Flint, S. S., 2015,
810 U-Pb zircon tuff geochronology from the Karoo Basin, South Africa: implications of
811 zircon recycling on stratigraphic age controls: International Geology Review, v. 57,
812 no. 4, p. 393-410.
813 Menning, M., Davydov, V. I., Devuyst, F.-X., Forke, H. C., Grunt, T. A., Hance, L., Heckel, P. H.,
814 Izokh, N. G., Jin, Y.-G., Jones, P. J., Kotlyar, G. V., Kozur, H. W., Nemyrovska, T. I.,
815 Schneider, J. W., Wang, X.-D., Weddige, K., Weyer, D., Work, D. M., Alekseev, A. S.,
816 and Chuvashov, B. I., 2006, Global timescale and regional stratigraphic reference
817 scales of central and west Europe, east Europe,Tethys,south China, and North
818 America as used in the Devonian–Carboniferous–Permian Correlation

819 Chart 2003 (DCP2003). Palaeogeography Palaeoclimatology Palaeoecology, v. 240, p. 318–
820 372.
821 Metcalfe, I., Crowley, J., Nicoll, R., and Schmitz, M., 2015, High-precision U-Pb CA-TIMS
822 calibration of middle Permian to lower Triassic sequences, mass extinction and
823 extreme climate-change in eastern Australian Gondwana: Gondwana Research, v.
824 28, no. 1, p. 61-81.
825 Rubidge, B. S., 2005, Re-uniting lost continents - Fossil reptiles from the ancient Karoo and
826 their wanderlust: South African Journal of Geology, v. 108, p. 135-172.
827 Rubidge, B. S., Modesto, S. P., Sidor, C., and Welman, J., 1999, Eunotosaurus africanus from
828 the Ecca-Beaufort contact in the Northern Cape - implications for Karoo Basin
829 development: South African Journal of Science, v. 95, p. 553-555.
830 Sirevaag, H., Ksienzyk, A., Jacobs, J., Dunkl, I., and Läufer, A., 2018, Tectono-Thermal
831 Evolution and Morphodynamics of the Central Dronning Maud Land Mountains, East
832 Antarctica, Based on New Thermochronological Data: Geosciences, v. 8, no. 11.
833 Steiner, M. B., 2006, The magnetic polarity time scale across the Permian-Triassic boundary:
834 Geological Society, London, Special Publications, v. 265, no. 1, p. 15-38.
835 Tohver, E., Lanci, L., Wilson, A., Hansma, J., and Flint, S., 2015, Magnetostratigraphic
836 constraints on the age of the lower Beaufort Group, western Karoo basin, South
837 Africa, and a critical analysis of existing U-Pb geochronological data: Geochemistry,
838 Geophysics, Geosystems, v. 16, no. 10, p. 3649-3665.
839 Torsvik, T. H., Van der Voo, R., Preeden, U., Mac Niocaill, C., Steinberger, B., Doubrovine, P.
840 V., van Hinsbergen, D. J. J., Domeier, M., Gaina, C., Tohver, E., Meert, J. G.,
841 McCausland, P. J. A., and Cocks, L. R. M., 2012, Phanerozoic polar wander,
842 palaeogeography and dynamics: Earth-Science Reviews, v. 114, no. 3-4, p. 325-368.
843 Turner, B. R., 1999, Tectonostratigraphical development of the upper Karoo foreland basin:
844 orogenic unloading versus thermally induced Gondwana rifting: Journal of African
845 Earth Sciences, v. 29, p. 215-238.
846 Wickens, H. D., 1994, Basin floor fan building turbidites of the southwestern Karoo Basin,
847 Permian Ecca Group, South Africa [PhD Unpublished PhD]: University of Port
848 Elizabeth, 233 p.
849 Williams, S. E., Müller, R. D., Landgrebe, T. C. W., and Whittaker, J. M., 2012, An open-
850 source software environment for visualizing and refining tectonic reconstructions
851 using high-resolution geological and geophysical data sets: GSA Today, v. 22, no. 4/5,
852 p. 4-9.
853 Wuertz, D., and Chalabi, Y., 2015, Package 'fGarch': Rmetrics—Autoregressive Conditional
854 Heteroskedastic Modelling. R Package Version 3010.82. https://cran.r-
855 project.org/web/packages/fGarch/fGarch.pdf.
856